An assessment of the role of surface sensible heat flux and the atmosphere inversion on the breakup time in a highly complex terrain

*

ABSTRACT

PENDING

1. Introduction

The formation of nocturnal Stable Boundary Layers (SBLs) and temperature inversions has important implications for urban areas, particularly those situated in complex terrain valleys. These range from physical processes, including the modulation of momentum, heat, and moisture exchange, to practical ones associated with pollutant accumulation near the surface, as well as the formation of Urban Heat Islands (UHI). Most pollutants emitted during the evening and throughout the night, together with those that return to the surface due to the top-down contraction of the residual layer, remain trapped in the valley atmosphere at least until the temperature inversion ceases (e.g. Doran et al. 2003; Schnitzhofer et al. 2009; Fernando et al. 2010; Saide et al. 2011; Liu et al. 2013; Hu et al. 2013; Rendón et al. 2014; Herrera-Mejía and Hoyos 2019). Depending on valley geomorphological characteristics, and the meteorological conditions surrounding the morning transition, pollutants may exit the valley atmosphere or recirculate. The latter could lead to a gradual deterioration of the air quality, and in some cases, to the onset of critical air pollution episodes (Anquetin et al. 1998; Angevine et al. 2001; Henne et al. 2004; Rendón et al. 2015; Czarnecka et al. 2019).

The inversion destruction, also referred to as the *inversion breakup* or the *inversion erosion*, is linked to the occurrence of the necessary and sufficient conditions for the development of the Convective Boundary Layer (CBL). The onset of the CBL leads to an efficient energy, moisture, and pollutant exchange between the surface and the free atmosphere (Schnitzhofer et al. 2009; Leukauf et al. 2015). Establishing under which conditions the nighttime inversion breaks up is not a trivial issue, especially for urbanized valleys, where the complexity of the terrain and the urban landscape directly influence the evolution of the SBL (Halios and Barlow 2018). Factors such as valley geometry, which induces topographic shading, soil water holding capacity and moisture, urban area fraction and roughness, and the overall valley circulation, are key in governing the inversion breakup in complex-urban environments. Some authors have explored the influence of these factors in the morning transition through both modeling (Whiteman and McKee 1982; Bader and McKee 1985; Colette et al. 2003; Whiteman et al. 2004; Zoumakis and Efstathiou 2006; Beare 2008; Rendón et al. 2014; Leukauf et al. 2015), and field experiments (Whiteman 1981; Angevine et al. 2001; Halios and Barlow 2018; Nadeau et al. 2018), highlighting the need for a better understanding and representation of the physical processes controlling the timing of the transition for improving numerical weather prediction and air pollution models (Angevine et al. 2001; Colette et al. 2003; Beare 2008; Rendón et al. 2014).

Whiteman (1981) and Whiteman and McKee (1982) categorized the inversion-breaking processes over mountainous valleys, predominantly rural, as a function of the interaction of two mechanisms. The first mechanism is considered local, and corresponds to the CBL growth from the bottom of the inversion resulting from radiative heating of the surface (Nadeau et al. 2018). The second mechanism depends on the valley circulation, in which the replacement of air masses at the valley bottom with air from the upper atmosphere through slope winds, causes the top of the inversion layer to collapse. Depending on the relative role of each of the described mechanisms, the breakup falls into three possible patterns, the first two resulting from the mechanisms previously mentioned, acting independently, and the third and last pattern to the simultaneous action of both mechanisms (Whiteman 1981). The idealized modeling experiments by Bader and McKee (1985) also suggest an essential role of both mechanisms in thermal inversion destruction.

Whiteman et al. (2004) reached different conclusions for high-latitude sinkholes, for which the evidence suggests that inversion destruction occurs mainly through subsidence warming, indirectly forced by the upslope flows. Valley geometry has a strong effect both on forcing the prevailing breakup pattern and on the timing of the inversion breakup, with inversions persisting longer in deeper valleys (Colette et al. 2003). The presence of extensive urban development over complex topography leads to alterations in the surface-atmosphere exchanges, enhancing valley floor heating through the formation of UHI. The induced heat due to the UHI may intensify the thermal turbulence production, accelerating the onset and growth of the CBL (Roth 2000; Rendón et al. 2015). Furthermore, slope winds tend to increase in magnitude as a consequence of strong temperature gradients appearing across the urbanized hills. The latter favors the inversion-breaking through the second and third breakup patterns. In addition to the above-mentioned processes, the evidence hints that wind shear plays a vital role in driving the Turbulent Kinetic Energy (TKE), and in the morning transition (Beare 2008).

From a broader perspective, regardless of terrain characteristics, and in terms of energy balance, the inversion breakup occurs when the total energy provided to the valley atmosphere (Q_{prov}, following the notation used in Leukauf et al. (2015)) via surface sensible heat flux (H) is equal to the energy required to erode the nocturnal SBL (Q_{req}) (Whiteman and McKee 1982; Angevine et al. 2001; Leukauf et al. 2016). Following the inversion breakup, the additional energy injected into the valley atmosphere is used, in part, to expand the CBL until the exchanges between the surface and the free atmosphere peak, resulting in a more efficient pollutant vertical transport. Leukauf et al. (2016) proposed a non-dimensional *breakup parameter* (B) defined as the ratio between Q_{req} and Q_{prov}, combining the effect of the atmospheric stability and the surface heating to assess the energy exchange processes. Leukauf et al. (2017) performed simulations, using the Weather Research and Forecasting (WRF) model (Skamarock et al. 2008), in different energy exchange scenarios characterized by different surface heating, initial atmospheric stability, and terrain geometry, to test the dependence of the exported heating on B. Leukauf et al. (2017) found that the amount of heat exported from the valley decreases exponentially as B increases and that there is a critical condition over which the complete SBL neutralization never occurs.

Despite the importance of the relationship between Q_{req} and Q_{prov} to understand the timing of the breakup and its potential modulating pollutant concentration, particularly for urbanized valleys, there is insufficient observational evidence of this effect. Recently Halios and Barlow (2018) studied the morning transition using ground-based remote sensing and in situ instrumentation in central London, finding that buoyant production of TKE at the surface and shear production in the upper half of the atmospheric boundary layer (ABL) erode the stable layer. They highlighted the importance of regional flows, such as low-level jets, in determining the urban boundary layer structure and growth.

The goal of this research is to gain insight into the above mentioned processes, based on the study of the trade-off between observed proxies of the energy provided to the valley atmosphere as H, and of the energy required to erode the nighttime inversion, both key in the inversion-breaking process in a low-latitude, highly urbanized valley. We also investigate the practical implications of the relative variability of these two proxies regarding the air quality and explore the efficiency of the energy injected into the atmosphere. Previous results suggest a substantial modulation of the local air pollutant concentration associated with ABL variability (Herrera-Mejía and Hoyos 2019). We analyze nine months of ground based remotely sensed thermodynamic profiles and in situ observations, including data from a microwave radiometer, a radar wind profiler, a 3D sonic anemometer, automatic weather stations, and air quality monitoring sensors. Furthermore, we evaluate the role of the valley circulation, primarily the vertical wind shear, and the regional meteorological conditions at different levels in the atmosphere, on the SBL erosion efficiency.

Section 2 presents a detailed description of the study area, the observational dataset, and the different thermodynamic proxies used for the assessment of Q_{req} and Q_{prov}. Section 3 includes the results of the relationship between the selected Q_{req} and the Q_{prov}. The section explores the SBL erosion efficiency, its dependence on local and regional meteorological conditions, the implications on air quality, and the intra-annual variability associated with the meteorological conditions in the valley. Finally, section 4 presents the most important conclusions of the study.

2. Methodology and observations

The observational assessment of turbulent fluxes, vertical structure of virtual potential temperature (θ_v) and wind speed, regional meteorology, and air quality measurements, allows studying the variability of the inversion breakup as a function of proxies representing Q_{req} and Q_{prov}, as well as the SBL erosion, and the impacts on local particulate matter (PM) concentration in a narrow, low-latitude valley.

The methodology includes i) the assessment of the magnitude and the intra-diurnal evolution of the proxies for Q_{req}, ii) the evaluation of the surface H as a proxy for Q_{prov}, iii) the study of the breakup time variability and the SBL erosion, iv) the assessment of the role of local and regional meteorology on the SBL erosion efficiency, and v) the estimation of the breakup time impact on the fine PM (PM2.5) concentration near the surface. We also examine the Q_{req}-Q_{prov} relationship from operational weather forecasts to explore whether the WRF model reproduces the observed relationship under realistic simulation conditions.

We use in situ and ground-based remote sensing observations, as well as satellite and reanalysis information from February 1 to November 21, 2018. Ground-based instrumentation is located along and across the region of interest, a highly urbanized low-latitude narrow valley. Although most of the data is available for a more extended time span, the analysis period is restricted by the availability of turbulent fluxes. In the analysis, all days with available data are considered, regardless of the meteorological conditions; in other words, we do not pre-select fair-weather days for the analysis. In a low-latitude environment, such days correspond to less than 1% of the data, which would restrict the study to very few cases, focusing on the exceptional circumstances and not the expected scenarios. The datasets comprise wet, transition, and dry seasons.

To better understand when, and under which conditions, the inversion breakup occurs, we start by assessing and comparing the characteristics of the stably stratified atmosphere of the Aburrá Valley before sunrise, using thermodynamic profiles obtained from a Microwave Radiometer (MWR), and the energy provided to the valley's atmosphere in the form of H. The thermodynamic profiles allow establishing a proxy for the amount of energy required to erode the stably stratified boundary layer, until the breakup occurs (Q_{req}). H is estimated using the eddy-covariance (EC) technique based on the turbulent fluctuations of the wind speed, temperature, and humidity measured using a 3D sonic anemometer. The overall approach combines high frequency measurements near the surface with macroscopic observations of the atmosphere in the vertical profile.

The inversion breakup assessment using a data analysis approach involves challenges associated with the spatial representativeness of each of the variables considered in the study. The latter is arguably the main reason why similar studies in the literature follow a modeling-based approach rather than an observational one. Turbulent fluxes estimated from in-situ observations generally represent the local-scale variability conditioned to the intrinsic heterogeneities of the terrain. In contrast, the thermodynamic profiles represent the macroscopic features of the atmosphere. Therefore, it is necessary to evaluate whether the observational datasets used in this study are suitable for the primary purpose and whether they reproduce the overall dynamics around the morning transition. Notwithstanding the potential limitations, the analysis using independent and different nature datasets constitutes a robust assessment of the inversion breakup process. The covariability among the datasets used in the study would imply a coherent response or connection among different atmospheric scales considered.

a. Geographical Context

The inversion breakup is studied using information from the Aburrá Valley. The valley is located in Colombia, in the Andes Cordillera between 6^{o}N and 6.5^{o}N and 75.3^{o}W and 75.6^{o}W (see Figure 1) and it is aligned predominantly south-to-north, south-to-northeast. The widest cross-section of the valley, from ridgeline to ridgeline, is 18.2 km, with a relatively flat section of approximately 8 km at the bottom. The narrowest section is around 3 km wide. The highest peak, approximately at 3110 m.a.s.l, is in the western hill. The basin outlet is at 1290 m.a.s.l.

From the point of view of turbulent exchanges, the complexity of the region is due to the rugged topography and the highly urbanized area. More than four million people are settled in an area of 1152 km^2. Additionally, the urban area reaches, in some cases, three-quarters of the hill-slope extension. The high population density in this geographic setting leads to several environmental challenges. These include the recurrent onset of critical air quality episodes due to the high demand for fossil fuels linked to motor vehicles and industries and the limited ventilation of the valley's atmosphere for pollutant dispersion.

b. Proxies for Q_{req}

An accurate determination of Q_{req} depends, first, on a precise theoretical definition of the time at which the atmosphere becomes neutrally stratified, establishing the initial conditions for the boundary layer growth phase. Following the work by Angevine et al. (2001), for flat terrain, numerous authors (e.g. Beare 2008; Nadeau et al. 2018) have defined the inversion breakup as the onset of the CBL, the time at which the nocturnal inversion in the surface layer has been eroded and turbulent eddies from the surface reach a certain depth (e.g., Angevine et al. (2001) used 200m above ground level). To some extent, the size of the eddies may be assessed observationally.

The appropriate selection of a proxy for the Q_{req} is not straightforward, mainly because such an index should adequately represent the entire volume of the valley's atmosphere. We consider thermodynamic indices such as the change of θ_v in the vertical at the lower-troposphere ($\Delta_z\theta_v$) and the Convective Inhibition Energy ($CINE$). $\Delta_z\theta_v$ has been extensively used as a proxy for the inversion strength (e.g. Whiteman 1981), considering that $\partial\theta_v/\partial z > 0$ corresponds to stable stratification, $\partial\theta_v/\partial z = 0$ to neutral conditions, and $\partial\theta_v/\partial z < 0$ to an unstable atmosphere (Peppler 1988; Curry and Webster 1999). Whiteman (1981) calculate $\Delta_z\theta_v$ as the difference between θ_v near the surface and at the top of the inversion. We consider $\Delta_z\theta_v$ for different atmospheric layers, where z corresponds to the height in meters above the surface. $\Delta_z\theta_v$ is computed as the difference between θ_v at height z and θ_v at height $z-\Delta z$, $\theta_v(z)-\theta_v(z-\Delta z)$. We consider $\Delta z = 200$m thick layers, with the only exception for $\Delta_{200}\theta_v$, computed as $\theta_v(200)-\theta_v(50)$ to avoid the potential effects of the roughness sublayer.

Furthermore, $CINE$ indicates the amount of energy inhibiting the updraft of air parcels, and is also an indirect measurement of the lower troposphere stability: as the stability of the atmosphere increases, $CINE$ becomes more negative. Conversely, unstable atmospheres correspond to $CINE$ nearing zero. $CINE$ is estimated as

$$CINE = \int_{SFC}^{LFC} g\frac{T_v' - T_v}{T_v}dz,$$

where LFC is the level of free convection, SFC is the surface level, T_v is the virtual temperature of the environment, and T_v' is the virtual temperature of the parcel (Peppler 1988). On occasions, the LFC largely exceeds the depth of the valley, where the trade winds advect eastward the H and the pollutants emitted at the surface. As a result, the amount of energy required for $CINE$ to become zero is larger than the amount of energy required to erode the stability within the valley. Also, the mechanisms that lead to changes in the thermodynamic profile above the valley may not be fully linked to the turbulent exchanges near the surface, but the forcing could be associated with the synoptic scale. To address this potential issue, and to have more control over the *CINE* integration height, the *LFC* is forced to a maximum of 1200 m, which is the average depth of the valley (see Figure 1). The modified index is referred to as $CINE_{1200}$.

The proxy for Q_{req}, on a daily time scale, corresponds to the maximum $\Delta_z\theta_v$, and the minimum *CINE* and $CINE_{1200}$ after sunrise, considering the topographic shading. $\Delta_z\theta_v$ and *CINE* are computed using thermodynamic profiles obtained using a MWR.

MWR DATA

An MP-3000A Microwave Radiometer (MWR), manufactured by Radiometrics, measured the vertical profiles of temperature and relative humidity in the Aburrá Valley up to 10 km from the top of SIATA's main operation center, approximately 60 m above the surface (see Figure 1a). The site is inside a sports complex, surrounded by different types of urban land uses. The MWR is a passive remote sensor that measures the radiation emitted by atmospheric gases using 31 different submillimeter-to-centimeter wavelengths. The MWR is useful for the retrieval of the thermodynamic state of the atmosphere at different levels, thus allowing the assessment of atmospheric stability. The MWR provides vertical profiles with a 2-minute temporal resolution and variable spatial resolution: 50 m from the surface to 500 m, 100 m up to 2 km, and 250 m up to 10 km. The lower-troposphere retrievals (below 4 km above the surface) are used to calculate the proxies for Q_{req}. The representativeness of the temperature and moisture profiles obtained using the MWR has been previously assessed using radiosonde measurements, showing high correlations for all the variables, including θ_v and $\Delta_z\theta_v$, in the lower troposphere (Roldán-Henao et al. 2020).

c. Inversion breakup time

Based on the different proxies for Q_{req}, the breakup time is assumed to have occurred when $\Delta\theta_v$ becomes zero after having been positive, or when $CINE = 0$ or relatively close to zero (we use $CINE < 20$ J kg^{-1} as a threshold). Figures 2a and b depict the steps used to assess the strength of the stability (Q_{req}) and the breakup time for a particular day, using $\Delta_{200}\theta_v$. In the example, the proxy for the strength of the stability is recorded as the maximum positive $\Delta_{200}\theta_v$ after sunrise, which corresponds to the gradient that must be neutralized to reach instability. According to Figure 2a, the value representing the strength of the instability for that particular date is 1.26 K. Figure 2b marks the breakup time, after 11:00 LT, corresponding to the moment when $\Delta_{200}\theta_v = 0$.

d. Proxy for Q_{prov}

The proxy used for the daily Q_{prov} (see Figures 2c) is the time-integrated surface H from the moment used to record the strength of the stability (maximum Q_{req} after sunrise) until the inversion breakup (see Figures 2a and b, respectively). The proxy is based on a modified version of the methodology presented in Angevine et al. (2001), which is based on the boundary layer growth equation in Garratt (1992). The methodology assumes that the temperature profile is mainly modified from the bottom as a function of sensible heating. This encroachment approach may introduce biases, given that it does not account for the θ_v profile modification in the lower troposphere, hence the stability modulation due to horizontal thermal advection. However, the evidence suggests that θ_v in the lower-troposphere, 500 m above ground, mainly varies as a result of vertical processes, with temperature changes lagging those in layers closer to the ground (not shown).

The H is estimated using the EC technique with a block-averaging period of 30 minutes. An EC tower equipped with a CSAT3 ultrasonic anemometer (Campbell Scientific) is used to obtain the three wind components (u', v', and w') and sonic temperature (T_s') with a sampling rate of 20Hz.

The instrument is installed 10 m above the surface, in a mast located next to the local airport (see Figure 1a). The absence of tall buildings in the surrounding area prevents the data from being strongly affected by the local circulation. Raw data are stored at full resolution in 24-hour files, and the statistical first- and second-order moments are calculated using 30-min block periods. After applying standard data quality controls (periods flagged by the instrument, checks for large data gaps and consistency limits, and data despiking), a coordinate double-rotation was applied for each 30-min interval to obtain the along-wind u and cross-wind v components. The latter ensures that the magnitude of the mean lateral and vertical components of the velocity vanishes for each of the averaging interval (e.g. McMillen 1988; Finnigan et al. 2003; Stiperski and Rotach 2016). Additional post-processing procedures include flux corrections (Webb et al. 1980; Moore 1986; Schotanus et al. 1983), and assessing of non-stationarity (following Foken and Wichura (1996)).A detailed description of the post-processing steps will be included in a separate publication (Herrera-Mejía et al. in preparation).

e. Role of breakup time in air quality

The breakup time is closely related to thermodynamically driven vertical dispersion processes. Consequently, the ABL neutralization may play a vital role in pollutant concentration. The assessment of the impact of the inversion breakup time on the air pollution near the surface of the valley is accomplished through the study of conditional probability density functions (CPDFs) of PM2.5 concentration as a function of the breakup time. In the Aburrá Valley, PM2.5 is the most critical air pollutant. All of the criteria air pollutants defined by the United States Environmental Protection Agency (U.S. EPA), except for lead, are routinely monitored in the region, in a 37-station comprehensive and accredited monitoring network. For this study, data from four in-situ PM2.5 stations equipped with a U.S. EPA Federal Equivalent Method (FEM) Met One Instruments BAM-1020 monitor is used. These stations are located along the base of the valley, some of them intentionally selected far from the location of the MWR and the CSAT3 (see Figure 1a), so as to indirectly test the representativeness of the proxies for Q_{req} and Q_{prov} for the entire valley. Retrievals from three Vaisala CL51 ceilometers (910 nm wavelength) are used to illustrate the structure of the vertical profile of aerosols in different Q_{req} scenarios. The ceilometer used is installed at the same site as the MWR (see Figure 1a). Ceilometers provide information regarding the laser-pulse energy backscattered by clouds and other atmospheric components, including aerosols, expressed as the backscattering attenuated coefficient (Emeis et al. 2009; Kambezidis et al. 2012; Wiegner et al. 2014).

f. Role of local and regional meteorology

One of the challenges in better understanding the ABL in complex terrain, and in particular, the morning transition, relates to the multiscale nature of the processes that modulate the phenomena. The overall behavior of the atmosphere at different levels exhibits signs of multiscale interaction, both in time and space. This is particularly true for the ABL over complex terrains, where the diurnal cycle, including the transition from the SBL to the CBL, is modulated by processes evolving on different temporal and spatial scales (e.g. Serafin et al. 2018; De Wekker and Kossmann 2015). The large-scale modulation of the ABL could occur directly through kinetic energy transfer between different scales of motion or indirectly via regional and large-scale changes in the conditions that favor or inhibit cloud formation, leading to surface radiative forcing. For this reason, it is essential to explore not only the turbulent exchanges, but also the potential role of the valley flow and the synoptic atmospheric circulation on the breakup time.

SYNOPTIC SCALE: REANALYSIS AND SATELLITE DATA

The methodology includes the evaluation of the contribution of the synoptic scale in modulating the morning transition. In the tropical environment, pressure patterns persist for very long periods, and the pressure and geopotential height gradients are typically weak, even during the passage of storm systems or perturbed weather in general. For this reason, the wind field is more useful than the pressure or geopotential height fields in describing the synoptic conditions in the tropics. In this regard, the velocity potential anomalies summarize the effect of synoptic-scale convection, allowing the tracking of upper-level divergence or convergence.

ERA5 reanalysis data (Hersbach et al. 2020) is used to calculate the velocity potential and the stream function corresponding to the reanalyzed wind fields. For the estimation of both variables, the wind field is separated into two components, the rotational ($\overrightarrow{V}_{rot}$) and the divergent component ($\overrightarrow{V}_{div}$) of the flow. The divergent winds are used to calculate a velocity potential (χ), satisfying that the winds flow out low potentials and their speed is proportional to their gradient ($\overrightarrow{V}_{div} = \nabla\chi$). In other words, χ is obtain as the solution to the equation $\nabla^2\chi = \nabla \cdot \overrightarrow{V}$ (Krishnamurti et al. 2013; Laing and Evans 2015). We also use the Outgoing Longwave Radiation (OLR) from the NOAA daily interpolated dataset (Liebmann and Smith 1996), to assess the role of synoptic forcing on the evolution of the intra-valley ABL.

In the assessment, three different atmospheric scenarios are considered, corresponding to cases when the nighttime inversion is strong (high Q_{req}) and i) the magnitude of the energy forcing provided to reach the morning transition via sensible heating is lower than the 33th percentile among all days considered in the study, ii) times when the energy provided to reach the transition is between the 33th and the 66th percentile, iii) and days for which the energy provided to the system, before reaching the transition, is larger than the 66th percentile.

Radar Wind Profiler (RWP) data

The RWP uses refractive index variations caused by changes in humidity, temperature, and pressure, to retrieve vertical profiles of winds (Lau et al. 2013). The Aburrá Valley wind profiler, a RAPTOR VAD-BL by DeTect Inc., works at a nominal frequency of 1290 MHz, reaching up to approximately 8 km above the surface under high humidity conditions. The RWP is designed to measure the wind profile in various operation modes that differ in their vertical resolution, as well as in the atmospheric domain sensed. The operation of the RWP includes two overlapping modes: in the higher resolution mode (60 m), the RWP retrieves the wind profile from 77 to 3500 m, and in the lower resolution mode (72 m), from 2500 to 8000 m. In the present study, only data from the higher resolution mode is used. The temporal resolution is five minutes.

WRF

We used the output of the operational daily 00Z WRF (version 3.7.1) 24-hour forecasts for three years. The model configuration includes three nested domains with 18 (191 x 191), 6 (82 x 118) , and 2 (136 x 136) *km* grid spacing, and 40 vertical levels up to 50 *hPa*. The description of the domains and the model setup are described in detail in Herrera-Mejía and Hoyos (2019).

3. Results

One of the main challenges in assessing the inversion breakup from an observational perspective is to ensure that measurements from in-situ sensors and ground-based remote sensing equipment represent the overall ABL variability in the valley. The latter is not only a challenge but a source of uncertainty in all ABL observational studies. While this challenge is difficult to overcome, it is possible to evaluate the holistic coherence and consistency among all variables in the dataset, and their capability to represent the ABL dynamics. Considering that most variables used in this study are obtained using different measurement techniques, high co-variability and interdependence in the dataset would indicate a skillful representation of the zeroth- and first-order valley dynamics, including the major spatial and temporal scales of variability.

Figure 3a depicts the interrelationship between the hourly H, $\Delta_{200}\theta_v$, and $CINE_{1200}$. Evidently, negative values of $\Delta_{200}\theta_v$ correspond to near-zero values of $CINE_{1200}$, and conversely, positive values of $\Delta_{200}\theta_v$ are associated with negative values of $CINE_{1200}$. The Pearson correlation between $\Delta_{200}\theta_v$ and $CINE_{1200}$ is -0.80. Figure 3b shows the correlations among all the Q_{req} proxies considered, including $\Delta_{200}\theta_v$, $\Delta_{800}\theta_v$, $\Delta_{Total}\theta_v$ ($\theta_v(1200)-\theta_v(50)$), $\Delta_{Sup}\theta_v$ ($\theta_v(800)-\theta_v(50)$)), $CINE$, $CINE_{1200}$, and $CINE_{1500}$. The magnitude of the linear correlations among all variables, except between $CINE$ and $\Delta_{Sup}\theta_v$, is over 0.6, emphasizing the high covariance of the virtual temperature in the lower levels of the troposphere, below LFC. This result serves as additional evidence of the strong dependence of the temperature profile on the surface heating, rather than on thermal advection.

Figure 3a shows that, for strong surface forcing to the ABL (high values of H), the likelihood of positive values of $\Delta_{200}\theta$ is very low. In other words, it is unlikely to have stable stratification when the heating is strong. Correspondingly, when H is larger than 150 Wm^{-2}, the average of $CINE_{1200}$ is -7.5 Jkg^{-1}. The large spread of the data at the bottom portion of the H-$\Delta_{200}\theta$ scatterplot is a consequence of the fact that the transition from a stable to an unstable atmosphere is a cumulative process, which does not depend exclusively on the magnitude of the surface forcing at a given time, but also on multiple additional factors. Furthermore, the observed relationship between H and the incoming radiation is very high, with a correlation of 0.89. Despite the different nature of the physical principles used to measure the different variables, the high covariability corresponds well with the expected behavior of the ABL, suggesting a clear link between the radiative forcing and H with the evolution of the nocturnal inversion within the valley. Based on these results, it is possible to follow the described observational approach. Additionally, considering the high correlations in 3b, the subsequent results are obtained using two proxies of Q_{req}: a near-surface stability proxy ($\Delta_{200}\theta_v$), and a lower-troposphere column integrated proxy ($CINE_{1200}$). Results using other proxies are similar and do not alter the main conclusions of this study.

a. Q_{req} *Vs.* Q_{prov}

Figures 4a and b show the relationship between Q_{req}, using $CINE_{1200}$ and $\Delta_{200}\theta_v$ as proxies, respectively, and Q_{prov} prior to the temperature profile neutralization, as defined. Each point on the scatterplot corresponds to a specific day between February and November 2018. Both diagrams show a remarkable correspondence between the two selected proxies for Q_{req}, providing evidence that Q_{prov} indeed is required to be higher when the magnitude of Q_{req} is large, regardless of the proxy used. The Q_{req}-Q_{prov} relationship is not linear. There appears to be a threshold in the strength of the inversion (Q_{req}), over which there is a considerable spread in the Q_{prov} before neutralization, implying that, in some cases, for the same Q_{req} the magnitude of Q_{prov} could be four to six times larger than usual before achieving SBL neutralization. The latter suggests the existence of a heating efficiency similar to the findings of Leukauf et al. (2017). This is explored further in subsection b.

Figure 5, similar to 4b but calculated using information from the WRF forecast runs. The diagrams for the WRF runs show, in general, a similar behavior to the observations, but with a larger spread Q_{prov} for large Q_{req}, hinting to a larger variability in the heating efficiency in the models.

The relationship observed in both diagrams in Figure 4 suggests a different state of the atmosphere for cases corresponding to the lower and upper parts of the scatter plots. To further explore this behavior, Figure 6 shows the comparison of the state of the atmosphere on two contrasting days, corresponding to the larger circles in Figure 4. The first case, with a high Q_{req}, corresponds to February 22, 2018 (see Figures 6a, b, c and, d), and the second case, with a low Q_{req}, corresponds to October 12, 2018 (lower panels) (see Figures 6e, f, g, and, h). The Figure includes the evolution of the θ_v profile, from 05:00 LT to 14:00 LT, the vertical profile of wind speed and wind direction, the ceilometer backscattering intensity profile from the surface up to 2.5 km, and finally, the hourly evolution of PM2.5 concentration.

The θ_v profiles reveal a strong nighttime inversion on February 22, 2018 (Figure 6a), resulting in a considerable amount of energy required to erode the SBL, a notably shallow ABL, and a late breakup time. The shallow ABL persisted after 14:00 as a direct consequence of the presence of high cloudiness (see Figure 6c) diminishing the incoming short-wave radiation to the surface. The RWP shows relatively strong north-easterly winds ($> 6ms^{-1}$) near the surface and up to approximately 400 m throughout the morning. The wind profile shows a reduction of the wind speed during the morning, above 400 m and up to the average depth of the valley (1000-1100 m) where the speed is higher due to the trade winds. In this case, the vertical exchanges within the valley atmosphere are restricted by the fact that no large eddies are being formed. In consequence, under these conditions, pollutants do not mix efficiently, as can be observed both in the relatively high ceilometer backscattering intensity and in the PM2.5 hourly concentration record (Figures 6c and d). On October 12, 2018, the atmospheric environment was diametrically opposite. Clear skies allowed for a swift transition from stable to neutral conditions, with an efficient ABL growth, and low backscattering intensities and PM2.5 concentration. An important feature is that winds within the ABL are considerably weaker in the morning time on October 12 than during the same period on February 22. A similar finding is reported in Halios and Barlow (2018), with a negative relationship between the growth rate of the mixing layer and the wind speed. More important than the magnitude of the wind speed, wind shear at the top of the ABL is higher on October 12 than on February 22. The latter could imply a larger ABL growth rate due to increased mechanical turbulence by shear production, leading to entrainment.

b. Heating efficiency

The previous results show a non-linear relationship between Q_{req} and Q_{prov}, and reflect an increase in Q_{prov} spread with the magnitude of Q_{req}, with implications for the breakup time. In a closed system, most sensible heating would be used to raise the lower troposphere temperature, expanding the ABL, and none of the energy would be exported to the free atmosphere. Under these idealized conditions, the relationship between Q_{req} and Q_{prov} would be bijective (one-to-one correspondence). If there are, however, atmospheric conditions that lead to heat being exported out of the valley's atmosphere, the heating efficiency would be diminished and most likely variable (e.g. Leukauf et al. 2017). Figure 7a shows, for different Q_{req} intervals, the 10th, 50th, and 90th Q_{prov} percentiles, with their corresponding regression functions. For the 10th and 50th percentiles, and up to approximately the 70th (not shown), Q_{req} and Q_{prov} follow a linear relationship. The latter suggests that, in 70% of the cases, the energy provided is mostly used to warm up the atmosphere within the valley: There is a linear relationship between Q_{req} and Q_{prov} for all the percentiles explored up to the 70th, and the changes in the slopes among different percentiles are not considerable. In contrast, from the 75th percentile onwards, Q_{prov} increases exponentially with Q_{req}.

Consequently, there appears to be a variable heating efficiency rate that is more evident for larger values of Q_{req}, with direct effects on the breakup time: observations suggest that, for all days with very low heating efficiency (large values of Q_{req} and Q_{prov} above the 70th percentile), the breakup occurs later than 13:00 LT. Therefore, it is essential to evaluate which mechanisms or atmospheric patterns are associated with low heating efficiency. Previous work (Angevine et al. 2001; Leukauf et al. 2016; Nadeau et al. 2018) link this possible leakage of energy with the valley circulation and the wind speed. The breaking times vary from 07:00 LT to approximately 16:00 LT, depending on the heat efficiency rate. When the heat efficiency is low (the upper part of the scatterplot), the nighttime inversion breaks late in the afternoon (after 14:00 LT), being unfavorable for pollutant dispersion as shown in the previous subsection.

ROLE OF LOCAL WIND SHEAR

To evaluate the potential influence of wind speed and vertical shear on the heating efficiency during the morning transition, we followed a composite analysis of these variables during three different subsets of dates. The three subsets of dates with contrasting heating efficiency correspond, in all cases, to values above the mean Q_{req}, and (i) Q_{prov} values below the 33th percentile, (ii) between the 33 and the 66th percentile, and (iii) above the 66th percentile (see Figure 7b). Figure 8a to c, and d to f, show the wind speed and the vertical wind shear, respectively, for the three subsets of dates. Area I corresponds to the lowest heating efficiency among the three subsets. Conversely, Area III corresponds to the highest heating efficiency (less energy provided to reach neutralization for a similar amount of Q_{req}). The evidence indicates that for lower wind speeds near the surface between 6:00 and 10:00 am LT, and more notably, for higher vertical wind shear, the erosion of the SBL occurs earlier and with less energy provided to the atmosphere in the form of surface H.

The observed enhanced shear corresponding to dates in the Area III set compared to the other sets is elevated, being maximum across the top of the SBL at the entrainment zone, rather than near the surface. Even under low wind speeds and with shear differences less than 1 ms^{-1}, the observational evidence suggests that shear production of TKE cannot be neglected. From the observations, the elevated shear appears to play an important role in enhancing the erosion of the SBL, likely by generating TKE.

Different authors have studied the role of elevated shear in the evolution of the CBL, most using a modeling approach and some using observations in flat terrains (e.g. Angevine 1999; Fedorovich et al. 2001; Conzemius and Fedorovich 2006; Fedorovich and Conzemius 2008; Halios and Barlow 2018). However, there is no consensus on whether a mean elevated shear enhances or suppresses entrainment. Conzemius and Fedorovich (2006) state that the boundary layer begins to grow due to increasing surface H and entrainment, with air from the free atmosphere being engulfed by convective thermals and becoming part of the boundary layer, a process that is modified by the presence of an elevated shear (Fedorovich et al. 2001). Compared to the effect of surface shear, the influence of elevated shear across the inversion on turbulence in the SBL and CBL is much less studied. It is clear that in addition to the often dominant buoyancy forcing, the CBL development is modulated by wind shear, which modifies considerably the internal structure of the lower troposphere. Therefore from this point of view, the timing of the breakup is modulated by the evolution of the surface H and the amount of mechanical turbulence due to wind shear.

Very few studies have explored the role of the elevated shear in a setting characterized by complex terrain and urbanization. The observational evidence presented here is not in agreement with the results presented in the theoretical work by Hunt and Durbin (1999). They found that the elevated shear prevented the entrainment process and the generation of TKE by deforming thermals so that they do not penetrate as effectively into the inversion, interfering with the entrainment, a process referred to as shear sheltering. However, in their work, they did not consider the potential effects of density stratification and the complex terrain setting. In their results, thermals do not overshoot their equilibrium level, and the CBL growth is slower. Fedorovich et al. (2001) and Conzemius and Fedorovich (2006) explore the directional effect of the elevated wind shear on the turbulent exchange across the capping inversion in Large Eddy Simulation (LES) experiments. In the numerical experiments, when the mixed-layer air has a higher momentum than the air above the inversion (negative elevated shear), CBL growth is enhanced contrary to the sheltering process described by Hunt and Durbin (1999). In contrast, in cases of positive shear, CBL growth is diminished. In contradiction to the mentioned modeling results, the evidence in Figure 8c and d shows a case where higher positive elevated shear (mixed-layer air has less momentum than the air above the inversion) leads to faster erosion of the SBL compared to when the positive elevated shear is weaker. The evidence suggests that the elevated shear does result in thermal damping at the inversion layer inhibiting the entrainment; conversely, it likely favors TKE generation and intensification of vertical transport of air from the mixed layer into the above-inversion region. The coincidence in the modeling studies and the results in Figure 8 lies in that the elevated shear appears to be much more important than the surface shear in the erosion of the SBL.

In addition to the vertical wind speed and wind shear, the magnitude of the upslope-downslope winds for the sets of days in Areas I, II, and III was also contrasted. The results do not show considerable and consistent differences among the three sets of dates.

ROLE OF SYNOPTIC CONDITIONS

The role of synoptic conditions on the ABL evolution over the Aburrá Valley is assessed considering the velocity potential, stream function, and OLR anomalies. The anomalies are computed as the difference between the daily average of the variable of intestest and the monthly average of the same variable. The velocity potential, OLR, and stream function average anomalies for the set of days corresponding to Areas I, II, and III in Figure 7b are shown in Figures 9, 10, and 11, respectively. Together, these variables represent the overall regional-scale convective activity.

The results suggest that, overall, for a similar Q_{req} values, the erosion of the SBL occurs not only faster but also with lower values of Q_{prov} (higher heating efficiency) for cases when the deep convection is inhibited regionally. Conversely, the SBL erosion is delayed, often until the afternoon, in scenarios when the regional deep convective activity is enhanced. In the latter case, the Q_{prov} values are three-four times larger than in the former conditions.

Figure 9a, b and c show, for Area I, positive velocity potential anomalies at 700 hPa over northern South America, weak anomalies at 500 hPa, and negative anomalies at 200 hPa, respectively. Such configuration indicates an enhancement of the deep convective activity in the region. In tropical South America, an enhanced deep convective activity often leads cloud formation. Figure Fig:OLR$_{A}$$nomaliesashowsnegativeOLRanomaliesassociatedwithAreaI, whichagreeswiththeobservedveloc$

The deep convective activity and OLR contrast for the dominant regional conditions in Area I vs. Area III suggests that the radiative forcing associated with deep convective clouds plays a dominant role in modulating the SBL erosion than the dynamical effect of the regional-scale convection. The average radiation between 06:00 and 12:00 LT for Area I is 401 Wm^{-2} and for Area III is 472 Wm^{-2}. It is expected that the 71 Wm^{-2} difference in radiation reaching the surface lead to a belated erosion of the SBL. However, the radiation difference in itself does not directly explain the larger Q_{prov} required in these cases, considering that Q_{req} at 06:00 LT is similar. Nevertheless, it does suggest that the extended SBL erosion period leads to inefficient heating of the ABL. It is likely that with longer erosion times, different processes such as heat export outside of the valley liked to upslope flow (e.g. Noppel and Fiedler 2002) lead to lower heating efficiency.

c. Variability of the breakup time and consequences for air quality

The absence of a marked top of the atmosphere radiation and surface air temperature seasonality in low-latitudes does not imply an insignificant valley-scale response to the annual climatology. In fact, the annual cycle in the tropics does impose variable large scale forcing, modulating the ABL variability. In the tropics, the seasonality of the Intertropical Convergence Zone (ITCZ) modulates local cloudiness, precipitation, and surface incident radiation, altering the characteristics of the nocturnal inversion and the erosion of the SBL.

Figure 12a shows a time-dependent clustering in the Q_{req} vs. Q_{prov} scatterplot around two different seasons (Feb-Jun and Jul-Nov). The latter suggests that the strength of the nighttime inversion, hence the energy required to erode the SBL, changes significantly throughout the year. Consequently, the inversion-breaking time also varies (see Figure 12b). Similar results are seen for the WRF forecasts runs (Figure 5). From February to mid-June, the proxy for Q_{req} is, on average, twice as large as that of the July-November period, and the inversion breakup occurs later in the day, in some cases even after 14:00 LT.

The timing of the atmospheric neutralization plays an important role in modulating air pollutant concentration. The PDFs for the daily average PM2.5 concentration, conditioned to breaking times occurring within four different hours during the day, suggest that, as the inversion breakup time occurs later in the day, the likelihood of higher PM2.5 concentrations increases. The concentration of aerosols in the valley's atmosphere is mainly influenced by the anthropogenic emissions at surface level and by the vertical dispersion of pollutants after the inversion breakup (e.g. Herrera-Mejía and Hoyos 2019). In cases of a late breakup, emissions accumulate within the SBL until thermal turbulence is activated, after which pollutants are lifted out of the valley. For the specific case of the Aburrá Valley, where atmospheric pollutant dispersion out of the valley is almost entirely thermodynamically driven, the magnitude of the turbulent exchange must be large enough for the ABL to reach the mountain peaks (1200 m.a.s.l.), where the pollutants are advected away far from the valley.

4. Conclusions

The variability and implications of the timing of the stable boundary layer breakup have been examined for a narrow valley located in the tropical Andes Cordillera using a combination of in-situ turbulent scale observations and remotely sensed macroscopic features of the local atmosphere. Given the topographic features of the region, it is imperative to understanding when and under which conditions the nocturnal inversion breaks up because it corresponds to the time when the exchanges between the surface and the free atmosphere intensify and reach their maximum, resulting in a more efficient pollutant vertical transport.

The assessment is based on an observational diagnostic framework developed to study the breakup time using proxies for the energy required to erode the atmospheric inversion (Q_{req}) and the amount of energy provided to the atmosphere via sensible heating (Q_{prov}), combining high frequency measurements near the surface with macroscopic observations of the atmosphere in the vertical profile. In this framework, the inversion breakup occurs when Q_{prov} via surface sensible heat flux (H) is equal to Q_{req}. Different thermodynamic indices were considered as proxies for Q_{req}, including changes of virtual potential temperature in the vertical at the lower-troposphere ($\Delta_z \theta_v$) and $CINE$. The inversion breakup assessment using the proposed framework involves challenges associated with the spatial representativeness of each of the variables considered in the study. However, the high covariability between the hourly H, $\Delta_{200}\theta_v$, $\Delta_{800}\theta_v$, $\Delta_{Total}\theta_v$ ($\theta_v(1200) - \theta_v(50)$), $\Delta_{Sup}\theta_v$ ($\theta_v(800) - \theta_v(50)$)), $CINE$, $CINE_{1200}$, and $CINE_{1500}$ indicates a coherent response among different atmospheric scales considered, hence serving as validation of the proposed methodology, regardless the limitations.

The relationship between Q_{req} and Q_{prov} allows concluding that Q_{prov} indeed is higher when the magnitude of Q_{req} is large, regardless of the proxy used. However, the observations indicate that the Q_{req}-Q_{prov} relationship is by no means simple. The evidence suggests the existence of non-constant heating efficiency for large values of Q_{req}, similar to the findings of Leukauf et al. (2017). In approximately 70% of the cases, the energy provided is mostly used to warm up the valley's atmosphere. In contrast, for approximately 25% of the cases, Q_{prov} increases exponentially with Q_{req}.

The vertical wind shear appears to be an important factor modulating the breakup time, hence the apparent heating efficiency. Higher vertical wind shear is linked to the earlier erosion of the SBL, with less energy provided to the atmosphere in the form of surface H. Moreover, the higher vertical wind shear does not occur near the surface. Instead, it is elevated, and it is maximum across the top of the SBL at the entrainment zone, suggesting that shear production of TKE cannot be neglected. The elevated shear, regardless of directional considerations, appears to play an essential role in enhancing the erosion of the SBL, likely by generating TKE. The evidence suggests that the timing of the breakup depends not only on the surface H but also on the amount of mechanical turbulence due to the elevated wind shear. The observational evidence presented here is important since there is no consensus on whether a mean elevated shear enhances or suppresses entrainment.

The synoptic conditions also play a role in the ABL evolution over the Aburrá Valley and breakup time. Velocity potential and OLR anomalies indicate that the erosion of the SBL occurs faster and with lower values of Q_{prov} (higher heating efficiency) when the deep convection is inhibited regionally. Conversely, the SBL erosion is delayed in scenarios when the regional deep convective activity is enhanced. The contrast in deep convective activity and OLR linked to variable heating efficiency suggests that the radiative forcing associated with deep convective clouds plays a dominant role in modulating the SBL erosion than the dynamical effect of the regional-scale convection. The difference in average radiation between 06:00 and 12:00 LT between cases with high and low heating efficiency was found to be approximately 70 Wm^{-2}. This difference is considerable and translates into considerably different breakup time, and with longer erosion times, various processes such as heat export outside of the valley through upslope flow reduce the heating efficiency.

The results suggest a large breakup time variability as a function of heating efficiency. In addition, the breakup time variability has been shown to have a profound impact on local air quality within the valley. The evidence indicates that, for later breakup times, the likelihood of higher PM2.5 concentrations increases considerably. In cases of a late breakup in complex terrains, anthropogenic emissions accumulate within the SBL until thermal turbulence is activated.

Acknowledgments. PENDING: OEAD and U Innsbruck, SIATA-AMVA, UNAL.., data... ORL, ERA... Interpolated OLR data provided by the NOAA/OAR/ESRL PSL, Boulder, Colorado, USA, from their Web site at

, all part of the meteorological and air-quality monitoring network of the Medellín and Aburrá Valley Early Warning System (SIATA, www.siata.gov.co)

References

Angevine, W. M., 1999: Entrainment results including advection and case studies from the flatland boundary layer experiments. *Journal of Geophysical Research: Atmospheres*, **104 (D24)**, 30 947–30 963, doi:https://doi.org/10.1029/1999JD900930, URL https://agupubs.onlinelibrary.wiley.com/doi/abs/10.1029/1999JD900930, https://agupubs.onlinelibrary.wiley.com/doi/pdf/10.1029/1999JD900930.

Angevine, W. M., H. K. Baltink, and F. C. Bosveld, 2001: Observations of the morning transition of the convective boundary layer. *Boundary-Layer Meteorology*, 209–227.

Anquetin, S., C. Guilbaud, and J.-P. Chollet, 1998: The Formation and Destruction of Inversion Layers within a Deep Valley. *Journal of Applied Meteorology*, **37 (12)**, 1547–1560, doi:10.1175/1520-0450(1998)037⟨1547:TFADOI⟩2.0.CO;2.

Bader, D. C., and T. B. McKee, 1985: Effects od shear, stability and valley Characteristics on the destruction of temperature inversions. *Journal of climate and applied meteorology*.

Beare, R. J., 2008: The Role of Shear in the Morning Transition Boundary Layer. *Boundary-Layer Meteorology*, 395–410, doi:10.1007/s10546-008-9324-8.

Colette, A., F. K. Chow, and R. L. Street, 2003: A Numerical Study of Inversion-Layer Breakup and the Effects of Topographic Shading in Idealized Valleys. *American Meteorological Society*, **96 (19)**, 1255–1272, doi:10.1103/PhysRevB.96.195117, 1707.06111.

Conzemius, R. J., and E. Fedorovich, 2006: Dynamics of Sheared Convective Boundary Layer Entrainment. Part I: Methodological Background and Large-Eddy Simulations. *Journal of the Atmospheric Sciences*, **63 (4)**, 1151–1178, doi:10.1175/JAS3691.1, URL https://doi.org/10.1175/JAS3691.1, https://journals.ametsoc.org/jas/article-pdf/63/4/1151/3490466/jas3691_1.pdf.

Curry, J., and P. Webster, 1999: *Thermodynamics of Atmospheres and Oceans*. International Geophysics, Elsevier Science, URL https://books.google.com.co/books?id=mdFzlFfWbiYC.

Czarnecka, M., J. Nidzgorska-lencewicz, and K. Rawicki, 2019: Temporal structure of thermal inversions in Ł eba (Poland). *Theoretical and Applied Climatology*, 1–13.

De Wekker, S. F. J., and M. Kossmann, 2015: Convective boundary layer heights over mountainous terrain—a review of concepts. *Frontiers in Earth Science*, **3**, 77, doi:10.3389/feart.2015.00077, URL https://www.frontiersin.org/article/10.3389/feart.2015.00077.

Doran, J., C. Berkowitz, R. Coulter, W. Shaw, and C. Spicer, 2003: The 2001 phoenix sunrise experiment: vertical mixing and chemistry during the morning transition in phoenix. *Atmospheric Environment*, **37 (17)**, 2365 – 2377, doi:https://doi.org/10.1016/S1352-2310(03)00134-1, URL http://www.sciencedirect.com/science/article/pii/S1352231003001341.

Emeis, S., K. Schäfer, and C. Münkel, 2009: Observation of the structure of the urban boundary layer with different ceilometers and validation by RASS data. *Meteorologische Zeitschrift*, **18 (2)**, 149–154, doi:10.1127/0941-2948/2009/0365, URL http://openurl.ingenta.com/content/xref?genre=article\&issn=0941-2948\&volume=18\&issue=2\&spage=149.

Fedorovich, E., and R. Conzemius, 2008: Effects of wind shear on the atmospheric convective boundary layer structure and evolution. *Acta Geophysica*, **56 (1)**, 114–141, doi:10.2478/s11600-007-0040-4, URL https://doi.org/10.2478/s11600-007-0040-4.

Fedorovich, E., F. T. M. Nieuwstadt, and R. Kaiser, 2001: Numerical and Laboratory Study of Horizontally Evolving Convective Boundary Layer. Part II: Effects of Elevated Wind Shear and Surface Roughness. *Journal of the Atmospheric Sciences*, **58 (6)**, 546–560, doi:10.1175/1520-0469(2001)058⟨0546:NALSOH⟩2.0.CO;2, URL https://doi.org/10.1175/1520-0469(2001)058⟨0546:NALSOH⟩2.0.CO;2, https://journals.ametsoc.org/jas/article-pdf/58/6/546/3458717/1520-0469(2001)058_0546_nalsoh_2_0_co_2.pdf.

Fernando, H. J. S., D. Zajic, S. Di Sabatino, R. Dimitrova, B. Hedquist, and A. Dallman, 2010: Flow, turbulence, and pollutant dispersion in urban atmospheres. *Physics of Fluids*, **22 (5)**, 051 301, doi:10.1063/1.3407662, URL https://doi.org/10.1063/1.3407662, https://doi.org/10.1063/1.3407662.

Finnigan, J. J., R. Clement, Y. Malhi, R. Leuning, and H. A. Cleugh, 2003: A RE-EVALUATIONOF LONG-TERM FLUX MEASUREMENT TECHNIQUES Part I : Averaging and Coordinate Rotation. *Boundary-Layer Meteorology*, **107 (1)**, 1–48, URL http://www.springerlink.com/index/J02R003J0376Q514.pdf.

Foken, T., and B. Wichura, 1996: Tools for quality assessment of surface-based flux measurements. *Agricultural and Forest Meteorology*, **78 (1-2)**, 83–105, doi:10.1016/0168-1923(95)02248-1.

Garratt, J. R., 1992: *The Atmospheric Boundary Layer*. CAMBRIDGE University Press, 331 pp.

Halios, C. H., and J. F. Barlow, 2018: Observations of the Morning Development of the Urban Boundary Layer Over London , UK , Taken During the ACTUAL Project. *Boundary-Layer Meteorology*, **166 (3)**, 395–422, doi:10.1007/s10546-017-0300-z.

Henne, S., and Coauthors, 2004: Quantification of topographic venting of boundary layer air to the free troposphere. *Atmospheric Chemistry and Physics*, **4 (2)**, 497–509, doi:10.5194/acp-4-497-2004, URL https://www.atmos-chem-phys.net/4/497/2004/.

Herrera-Mejía, L., and C. D. Hoyos, 2019: Characterization of the Atmospheric Boundary Layer in a Narrow Tropical Valley Using Remote Sensing and Radiosonde Observations, and the WRF Model: The Aburrá Valley Case Study. *Quarterly Journal of the Royal Meteorological Society*, 35, doi:10.1002/qj.3583, URL https://onlinelibrary.wiley.com/doi/abs/10.1002/qj.3583.

Hersbach, H., and Coauthors, 2020: The era5 global reanalysis. *Quarterly Journal of the Royal Meteorological Society*, **146 (730)**, 1999–2049, doi:10.1002/qj.3803, URL https://rmets.onlinelibrary.wiley.com/doi/abs/10.1002/qj.3803, https://rmets.onlinelibrary.wiley.com/doi/pdf/10.1002/qj.3803.

Hu, X.-M., P. M. Klein, M. Xue, J. K. Lundquist, F. Zhang, and Y. Qi, 2013: Impact of low-level jets on the nocturnal urban heat island intensity in oklahoma city. *Journal of Ap-*

plied Meteorology and Climatology, **52 (8)**, 1779–1802, doi:10.1175/JAMC-D-12-0256.1, URL https://doi.org/10.1175/JAMC-D-12-0256.1, https://doi.org/10.1175/JAMC-D-12-0256.1.

Hunt, J., and P. Durbin, 1999: Perturbed vortical layers and shear sheltering. *Fluid Dynamics Research*, **24 (6)**, 375 – 404, doi:https://doi.org/10.1016/S0169-5983(99)00009-X, URL http://www.sciencedirect.com/science/article/pii/S016959839900009X.

Kambezidis, H. D., A. G. Paliatsos, N. Kappos, and B. Kasselouri, 2012: A Case of African Dust Transport over Athens Captured by a Ceilometer. *Advances in Meteorology, Climatology and Atmospheric Physics*, 1245–1250, doi:10.1007/978-3-642-29172-2, URL http://link.springer.com/10.1007/978-3-642-29172-2.

Krishnamurti, T., L. Stefanova, and V. Misra, 2013: *Tropical Meteorology: An Introduction*. Springer Atmospheric Sciences, Springer New York, URL https://books.google.com.co/books?id=dfa8BAAAQBAJ.

Laing, A., and J. L. Evans, 2015: *Introduction to tropical meteorology, 2nd Edition*. The COMET Program, URL http://www.meted.ucar.edu/tropical/textbook_2nd_edition/index.htm.

Lau, E., and Coauthors, 2013: The DeTect Inc. RAPTOR VAD-BL Radar Wind Profiler. *Journal of Atmospheric and Oceanic Technology*, **30**, 1978–1984, doi:10.1175/JTECH-D-12-00259.1, URL http://journals.ametsoc.org/doi/abs/10.1175/JTECH-D-12-00259.1.

Leukauf, D., A. Gohm, and M. W. Rotach, 2016: Quantifying horizontal and vertical tracer mass fluxes in an idealized valley during daytime. *Atmospheric Chemistry and Physics*, 13 049–13 066, doi:10.5194/acp-16-13049-2016.

Leukauf, D., A. Gohm, and M. W. Rotach, 2017: Toward generalizing the impact of surface heating, stratification, and terrain geometry on the daytime heat export from an idealized valley. *Journal of Applied Meteorology and Climatology*, **56 (10)**, 2711–2727, doi: 10.1175/JAMC-D-16-0378.1.

Leukauf, D., A. Gohm, M. W. Rotach, and J. S. Wagner, 2015: The impact of the temperature inversion breakup on the exchange of heat and mass in an idealized valley: Sensitivity to the radiative forcing. *Journal of Applied Meteorology and Climatology*, **54 (11)**, 2199–2216, doi: 10.1175/JAMC-D-15-0091.1.

Liebmann, B., and C. A. Smith, 1996: Description of a complete (interpolated) outgoing longwave radiation dataset. *Bulletin of the American Meteorological Society*, **77 (6)**, 1275–1277, URL http://www.jstor.org/stable/26233278.

Liu, X. G., and Coauthors, 2013: Formation and evolution mechanism of regional haze: a case study in the megacity beijing, china. *Atmospheric Chemistry and Physics*, **13 (9)**, 4501–4514, doi:10.5194/acp-13-4501-2013, URL https://www.atmos-chem-phys.net/13/4501/2013/.

McMillen, R. T., 1988: An eddy correlation technique with extended applicability to non-simple terrain. *Boundary-Layer Meteorology*, **43 (3)**, 231–245, doi:10.1007/BF00128405, URL https://doi.org/10.1007/BF00128405.

Moore, C. J., 1986: Frequency response corrections for eddy correlation systemns. *Boundary-Layer Meteorology*, **37**, 17–35.

Nadeau, D. F., H. J. Oldroyd, E. R. Pardyjak, N. Sommer, S. W. Hoch, and M. B. Parlange, 2018: Field observations of the morning transition over a steep slope in a narrow alpine valley. *Environmental Fluid Mechanics*, 1–22, doi:10.1007/s10652-018-9582-z, URL https://doi.org/10.1007/s10652-018-9582-z.

Noppel, H., and F. Fiedler, 2002: Mesoscale heat transport over complex terrain by slope winds – a conceptual model and numerical simulations. *Boundary-Layer Meteorology*, **104 (1)**, 73–97, doi:10.1023/A:1015556228119, URL https://doi.org/10.1023/A:1015556228119.

Peppler, R. A., 1988: A review of static stability indices and related thermodynamic parameters. Tech. rep., Illinois State Water Survey.

Rendón, A. M., J. F. Salazar, C. A. Palacio, and V. Wirth, 2015: Temperature inversion breakup with impacts on air quality in urban valleys influenced by topographic shading. *Journal of Applied Meteorology and Climatology*, **54 (2)**, 302–321, doi:10.1175/JAMC-D-14-0111.1.

Rendón, A. M., J. F. Salazar, C. A. Palacio, V. Wirth, and B. Brötz, 2014: Effects of urbanization on the temperature inversion breakup in a mountain valley with implications for air quality. *Journal of Applied Meteorology and Climatology*, **53 (4)**, 840–858, doi:10.1175/JAMC-D-13-0165.1.

Roldán-Henao, N., C. D. Hoyos, L. Herrera-Mejía, and A. Isaza, 2020: An investigation of the precipitation net effect on the particulate matter concentration in a narrow valley: Role of lower-troposphere stability. *Journal of Applied Meteorology and Climatology*, **59 (3)**, 401–426, doi:10.1175/JAMC-D-18-0313.1, URL https://doi.org/10.1175/JAMC-D-18-0313.1, https://doi.org/10.1175/JAMC-D-18-0313.1.

Roth, M., 2000: Review of atmospheric turbulence over cities. *Quarterly Journal of the Royal Meteorological Society*, **126 (564)**, 941–990, doi:10.1256/smsqj.56408.

Saide, P. E., G. R. Carmichael, S. N. Spak, L. Gallardo, A. E. Osses, M. A. Mena-Carrasco, and M. Pagowski, 2011: Forecasting urban pm10 and pm2.5 pollution episodes in very stable nocturnal conditions and complex terrain using wrf–chem co tracer model. *Atmospheric*

Environment, **45 (16)**, 2769 – 2780, doi:https://doi.org/10.1016/j.atmosenv.2011.02.001, URL http://www.sciencedirect.com/science/article/pii/S1352231011001178.

Schnitzhofer, R., and Coauthors, 2009: A multimethodological approach to study the spatial distribution of air pollution in an alpine valley during wintertime. *Atmospheric Chemistry and Physics*, **9 (10)**, 3385–3396, doi:10.5194/acp-9-3385-2009, URL https://www.atmos-chem-phys.net/9/3385/2009/.

Schotanus, P., F. T. Nieuwstadt, and H. A. De Bruin, 1983: Temperature measurement with a sonic anemometer and its application to heat and moisture fluxes. *Boundary-Layer Meteorology*, **26 (1)**, 81–93, doi:10.1007/BF00164332.

Serafin, S., and Coauthors, 2018: Exchange processes in the atmospheric boundary layer over mountainous terrain. *Atmosphere*, **9 (3)**, doi:10.3390/atmos9030102, URL https://www.mdpi.com/2073-4433/9/3/102.

Skamarock, W. C., J. B. Klemp, J. Dudhia, D. O. Gill, D. M. Barker, W. Wang, and J. G. Powers, 2008: A description of the advanced research wrf version 3. ncar technical note -475+str.

Stiperski, I., and M. W. Rotach, 2016: On the measurement of turbulence over complex mountainous terrain. *Boundary-Layer Meteorology*, **159 (1)**, 97–121, doi:10.1007/s10546-015-0103-z, URL https://doi.org/10.1007/s10546-015-0103-z.

Webb, E. K., G. I. Pearman, and R. Leuning, 1980: Correction of flux measurements for density effects due to heat and water vapour transfer. *Quarterly Journal of the Royal Meteorological Society*, **106 (447)**, 85–100, URL http://onlinelibrary.wiley.com/doi/10.1002/qj.49710644707/abstract{\%}0Apapers3://publication/uuid/D93C7190-B5B7-4657-9C9F-5868BDE5DFED.

Whiteman, C. D., 1981: Breakup of temperature inversions in deep mountain valleys: Part I. Observations. 270–289 pp., doi:10.1175/1520-0450(1983)022⟨1314:COOTII⟩2.0.CO;2.

Whiteman, C. D., and T. B. McKee, 1982: Breakup of temperature inversions in deep mountain valleys: Part II. Thermodynamic Model. *Journal of Applied Meteorology*, 290 – 302.

Whiteman, C. D., B. Pospichal, S. Eisenbach, P. Weihs, C. B. Clements, R. Steinacker, E. Mursch-Radlgruber, and M. Dorninger, 2004: Inversion Breakup in Small Rocky Mountain and Alpine Basins. *Journal of Applied Meteorology*, **43 (8)**, 1069–1082, doi:10.1175/1520-0450(2004)043⟨1069:ibisrm⟩2.0.co;2.

Wiegner, M., and Coauthors, 2014: What is the benefit of ceilometers for aerosol remote sensing? An answer from EARLINET. *Atmospheric Measurement Techniques*, **7**, 1979–1997, doi:10.5194/amt-7-1979-2014.

Zoumakis, N. M., and G. A. Efstathiou, 2006: Parameterization of inversion breakup in idealized valleys. Part I: The adjustable model parameters. *Journal of Applied Meteorology and Climatology*, **45 (4)**, 600–608, doi:10.1175/JAM2353.1.

LIST OF FIGURES

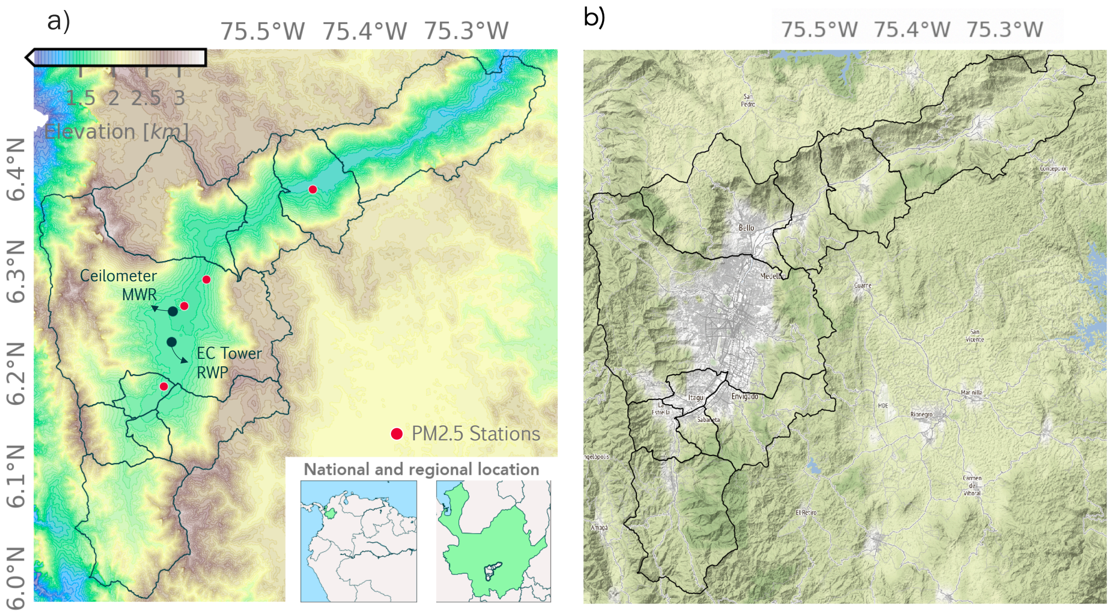

FIG. 1. a) Geographical context of the Aburrá Valley, located in northern South America, Colombia, Department of Antioquia, north of the equator. The map shows, in brown to blue colors, the height above sea level, the main topographic features in the region, and the location of the sensors used in the study, including a microwave radiometer (MWR), a ceilometer, air quality monitoring stations, and a sonic anemometer. b) Hillshade relief map of the study area, displaying the urbanized areas of the valley, in gray.

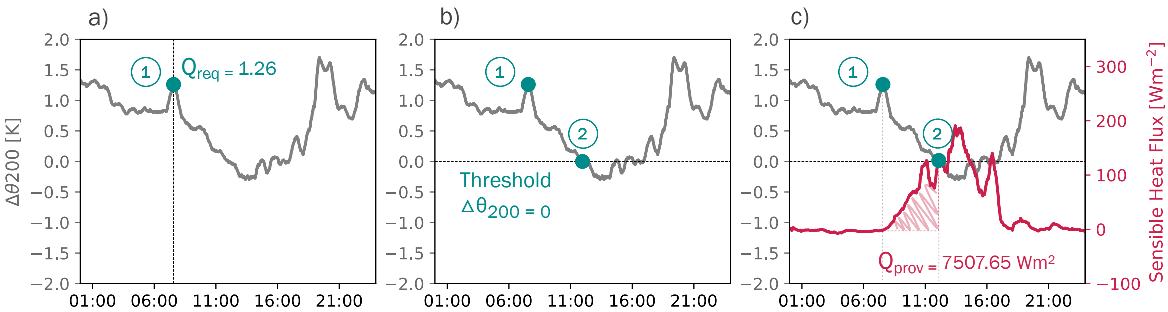

FIG. 2. Graphical representation of the steps used to assess the strength of the stability (Q_{req}) and the breakup time for a particular day. This example uses $\Delta_{200}\theta_v$ as a proxy for Q_{req}, but a similar methodology is followed for other proxies. a) The proxy for the strength of the stability is recorded as the maximum positive $\Delta_{200}\theta_v$ after sunrise. b) Detection of the breakup time. c) Estimation of Q_{prov} as the time integral of H from the moment used to record the strength the stability (maximum Q_{req} after sunrise) until the inversion breakup.

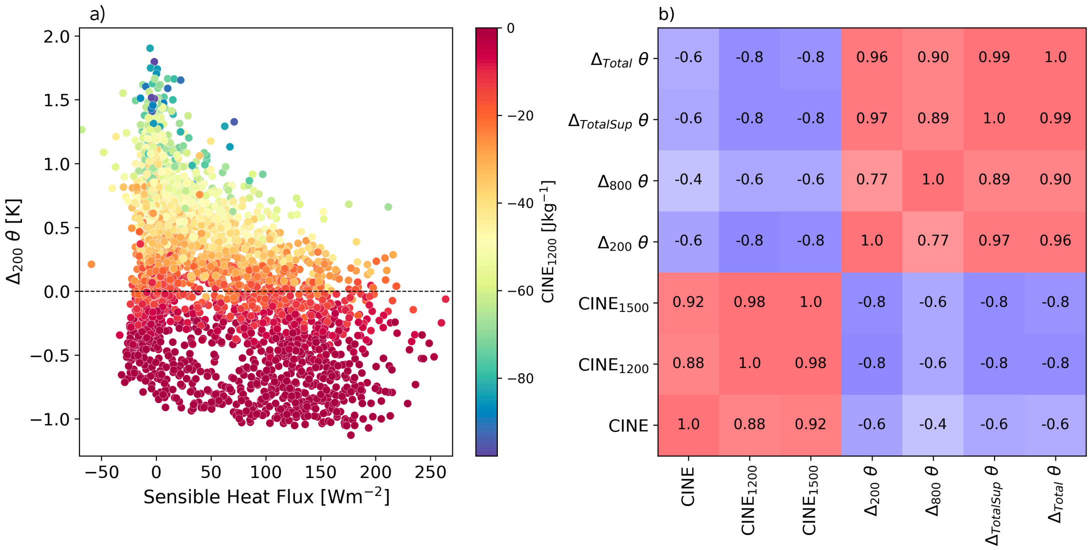

FIG. 3. a) Observed covariability between H, $\Delta_{2000}\Theta$, and $CINE_{1200}$. Colors indicate that magnitudes of $CINE_{1200}$. The figure shows $CINE_{1200}$ increases (less negative) as the slope of the potential temperature profile $\Delta_{200}\theta_v$ changes from positive to negative, reaching its highest negative values when the forcing is low and $\Delta\theta 200$ is close to zero. b) Correlation matrix among all the Q_{req} proxies considered, including $\Delta_{200}\theta_v$, $\Delta_{800}\theta_v$, $\Delta_{Total}\theta_v$ ($\theta_v(1200) - \theta_v(50)$), $\Delta_{Sup}\theta_v$ ($\theta_v(800) - \theta_v(50)$)), $CINE$, $CINE_{1200}$, and $CINE_{1500}$.

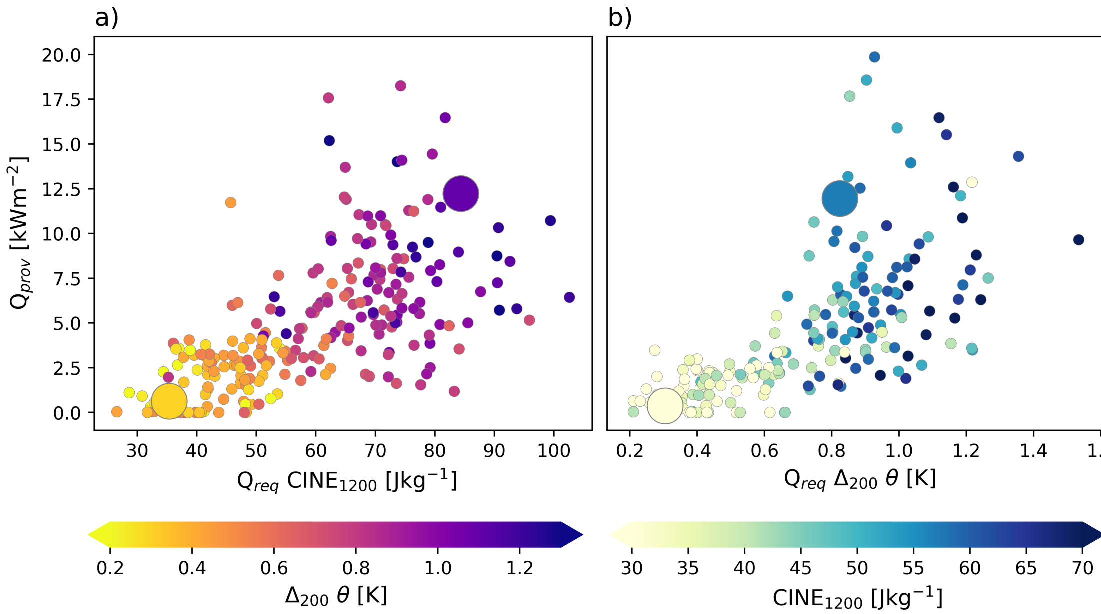

FIG. 4. Scatter plots of the selected proxies of Q_{req}, a) $CINE_{1200}$ and b) $\Delta_{200}\theta_v$, and Q_{prov} as retrieved following the methodology in Figure 2. It is important to note that panel a) uses $-CINE_{1200}$. Each point in the scatter plots corresponds to a specific day between February and November 2018. The larger circles correspond to two contrasting days, February 22, 2018, and October 12, 2018 as described in the text.

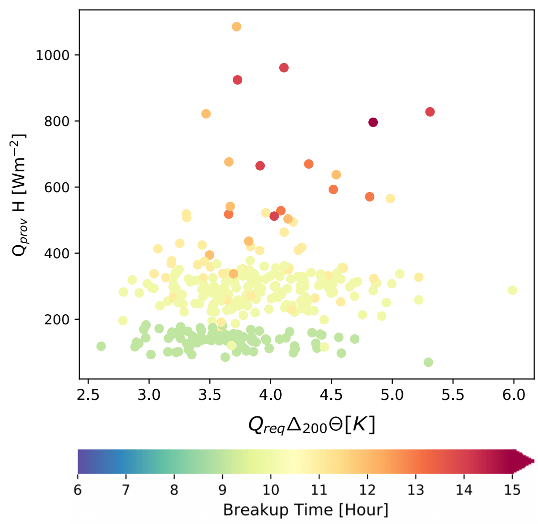

828 FIG. 5. Scatter plots of $\Delta_{200}\theta_v$ and Q_{prov} following the methodology in Figure 2 using information from the
829 WRF forecast runs. The colors correspond to the breakup time in each case.

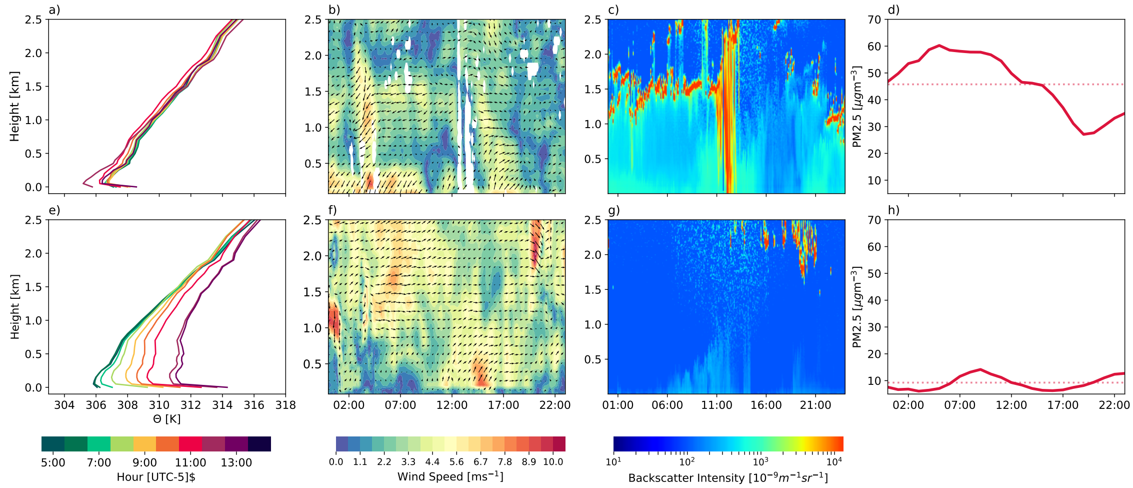

FIG. 6. The panels show different atmospheric variables for two contrasting days. The upper panels correspond to February 22, 2018, and the lower panels to October 12, 2018. Panels a) and e) show the hourly evolution of the θ_v profile, from 05:00 LT to 14:00 LT. Panels b) and f) the vertical profiles of wind speed and direction. Panels c) and g) the ceilometer backscattering intensity profiles from the surface up to 2.5 km. Panels d) and h) the hourly evolution of PM2.5 concentration.

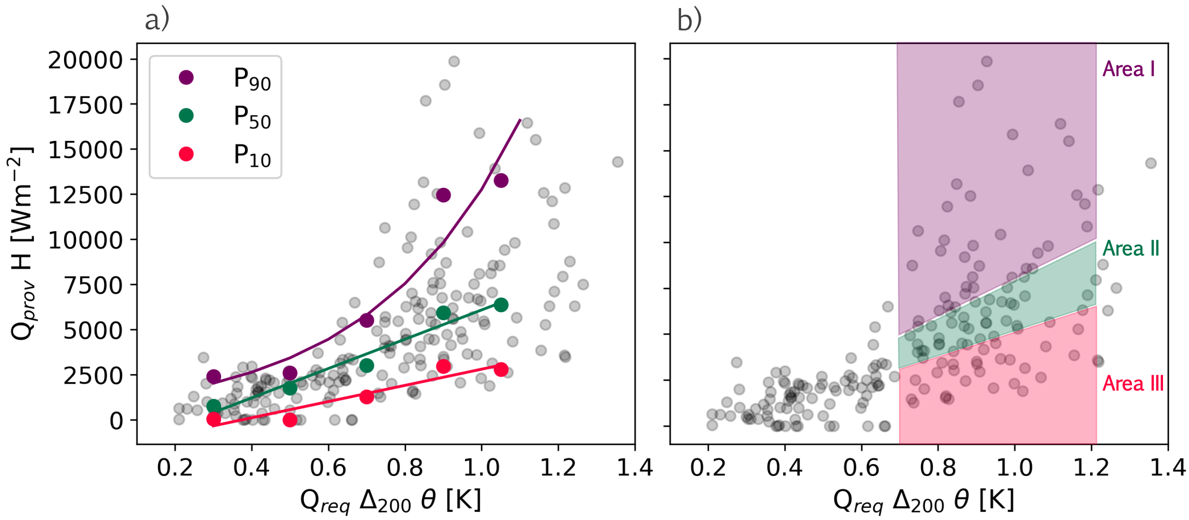

FIG. 7. a) Regression functions for the 10th, 50th, and 90th Q_{prov} percentiles and Q_{req}. The regression functions are obtained for each percentile after binning the Q_{req} in intervals, and obtaining the corresponding 10th, 50th, and 90th Q_{prov} percentile for each of the intervals. b) Selection of three graphical areas in the Q_{req}-Q_{prov} diagram for composite analyses. The areas correspond to cases above the mean Q_{req}, and below the 33th Q_{prov} percentile (Area III), between the 33th and the 66th percentile (Area II) and above the 66th percentile (Area I).

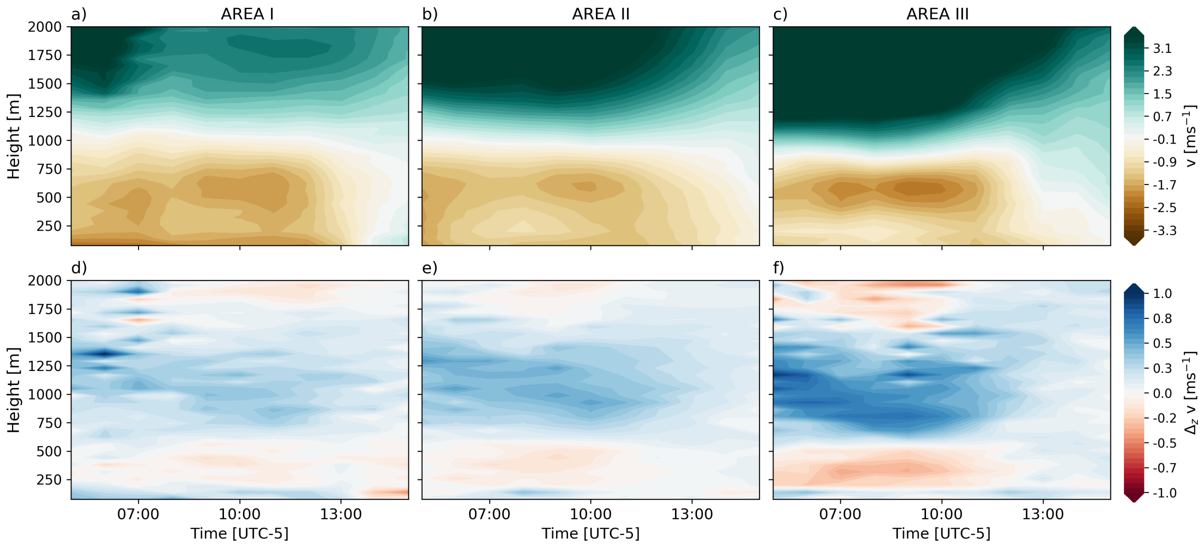

841 FIG. 8. Temporal evolution of the profiles of wind speed (a,b,c) and vertical wind shear (d,e,f) from 05:00 LT
842 to 14:00 LT, for each set (Atea I, II, and III) defined in Figure 7.

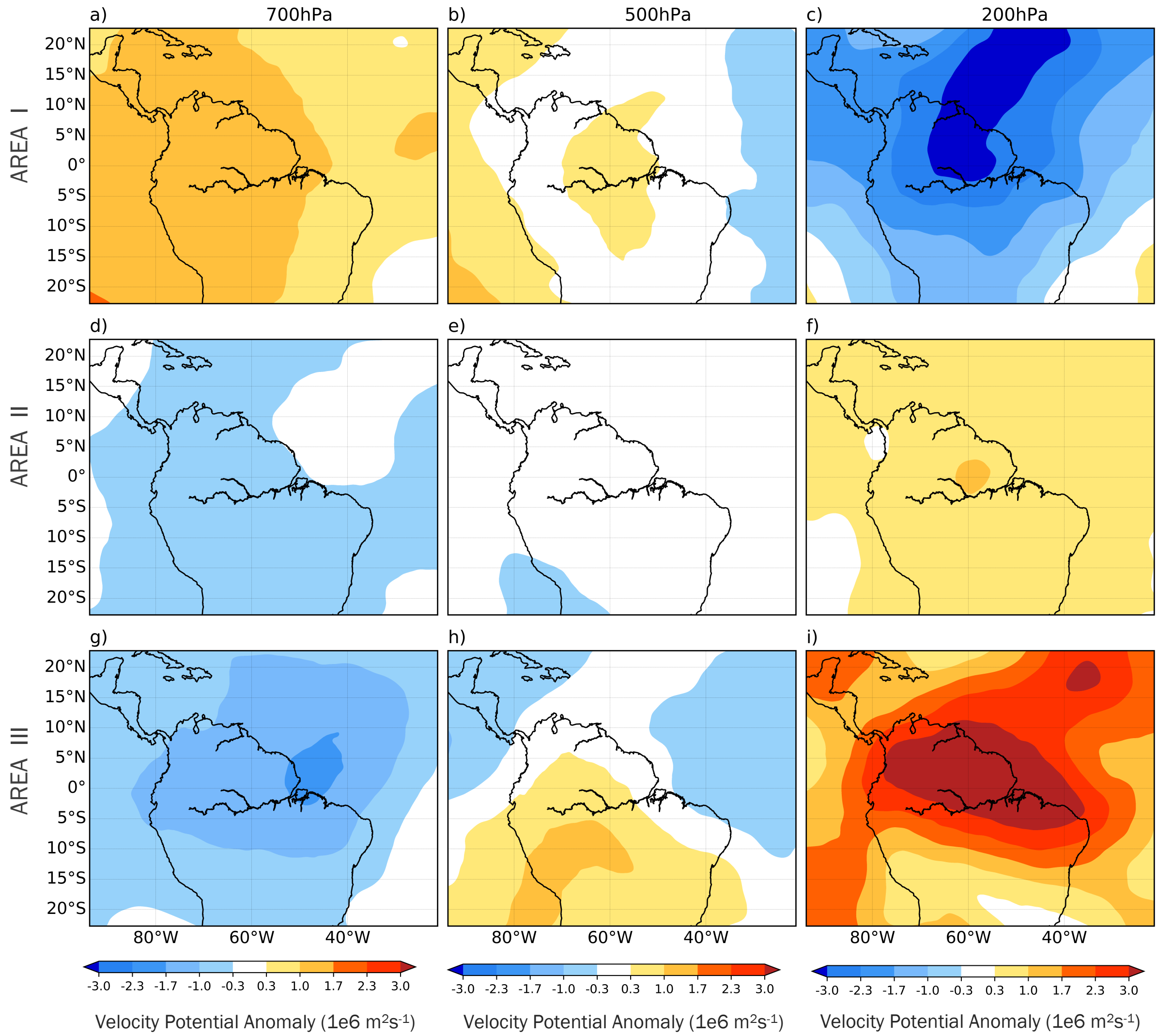

843 FIG. 9. Average velocity potential anomalies for different atmospheric leves and for each of the set of dates (Areas I, II, and III) selected in Figure 7b. The top row corresponds to Area I, the middle row to Area II, and the bottom row to Area III. Panels a), d), and c) correspond to anomalies at 700 hPa. Panels b), e), and h) to anomalies at 500 hPa. Panels c), f), and i) to anomalies at 200 hPa.

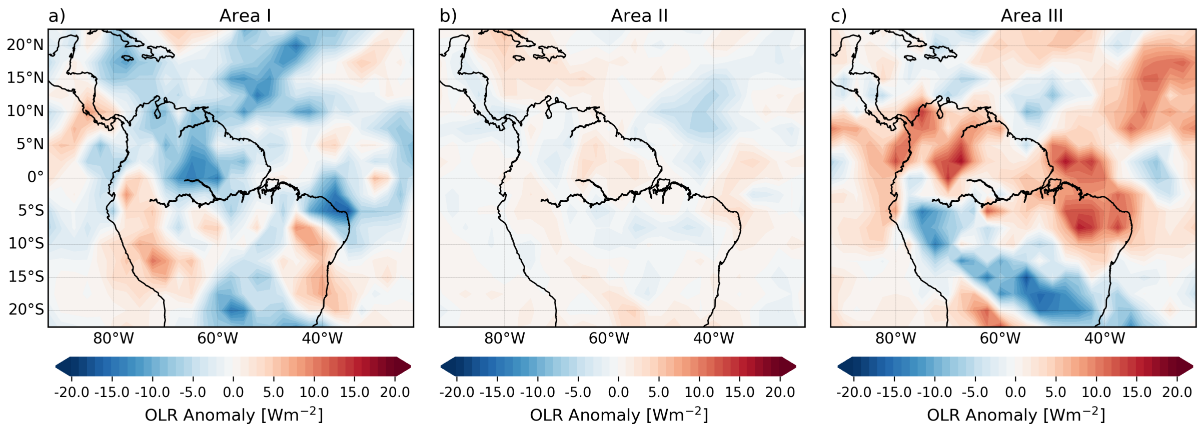

FIG. 10. Similar to Figure 9 but for average OLR anomalies.

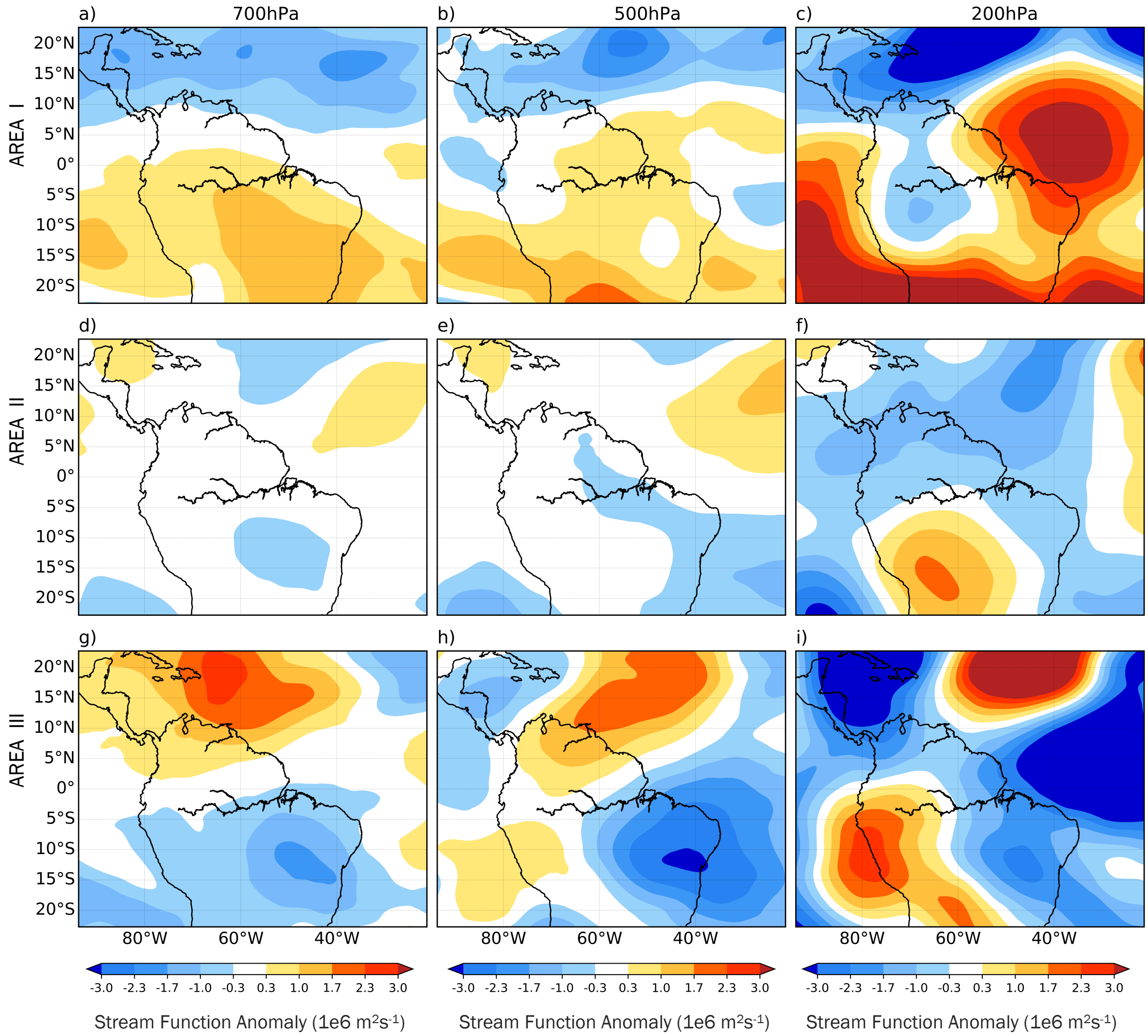

FIG. 11. Similar to Figure 9 but for average stream function anomalies.

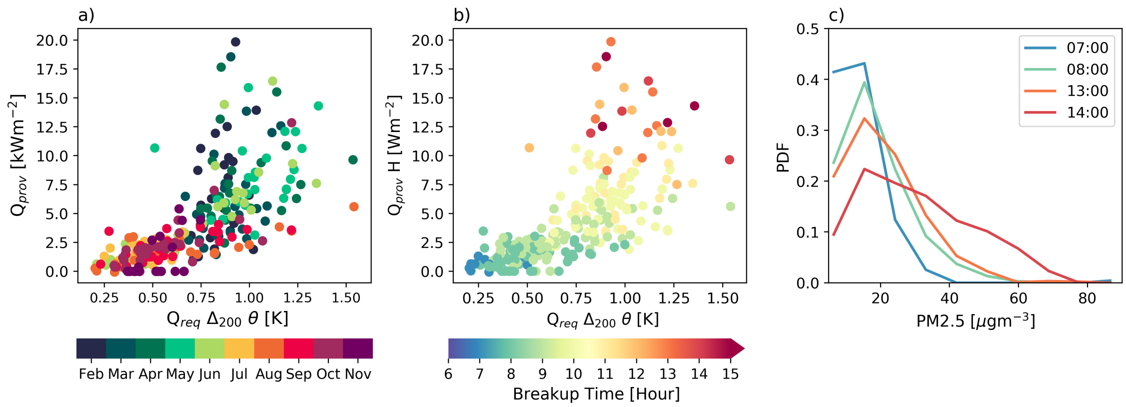

FIG. 12. a) Evidence of seasonal dependence of the Q_{req} and heating efficiency. b) Evidence of breakup time variability as a function of Q_{req} and heating efficiency. c) Probability density functions of PM2.5 concentrations in the atmosphere near the surface as a function of breakup time.